Soft Matter

# Towards Mechanical Characterization of Granular Biofilms by Optical Coherence Elastography Measurements of Circumferential Elastic Waves



| | |
|---|---|
| Journal: | *Soft Matter* |
| Manuscript ID | SM-ART-04-2019-000739.R1 |
| Article Type: | Paper |
| Date Submitted by the Author: | 08-Jun-2019 |
| Complete List of Authors: | Liou, Hong-Cin; Northwestern University, Mechanical Engineering<br>Sabba, Fabrizio; Northwestern University, Civil and Environmental Engineering<br>Packman, Aaron; Northwestern University, Civil and Environmental Engineering<br>Rosenthal, Alex; Northwestern University, Civil and Environmental Engineering<br>Wells, George; Northwestern University, Civil and Environmental Engineering<br>Balogun, Oluwaseyi; Northwestern University, Mechanical Engineering; Northwestern University, Civil and Environmental Engineering |
| | |

# Towards Mechanical Characterization of Granular Biofilms by Optical Coherence Elastography Measurements of Circumferential Elastic Waves

*Hong-Cin Liou[1], Fabrizio Sabba[2], Aaron I. Packman[2], Alex Rosenthal[2], George Wells[2], Oluwaseyi Balogun[1,2*]*

[1]Mechanical Engineering Department, Northwestern University, Evanston, IL 60208

[2]Civil and Environmental Engineering Department, Northwestern University, Evanston, IL 60208

***Corresponding author:**

Oluwaseyi Balogun, Phone: +1 847-491-3054; e-mail: o-balogun@u.northwestern.edu

## ABSTRACT

Microbial granular biofilms are spherical, multi-layered aggregates composed of communities of bacterial cells encased in a complex matrix of hydrated extracellular polymeric substances (EPS). While granular aggregates are increasingly used for applications in industrial and municipal wastewater treatment, their underlying mechanical properties are poorly understood. The challenges of viscoelastic characterization for these structures are due to their spherical geometry, spatially heterogeneous properties, and their delicate nature. In this study, we report a model-based approach for nondestructive characterization of viscoelastic properties (shear modulus and shear viscosity) of alginate spheres with different concentrations, which was motivated by our measurements in granular biofilms. The characterization technique relies on experimental measurements of circumferential elastic wave speeds as a function of frequency in the samples using the Optical Coherence Elastography (OCE) technique. A theoretical model was developed to estimate the viscoelastic properties of the samples from OCE data through inverse analysis. This work represents the first attempt to explore elastic waves for mechanical characterization of granular biofilms. The combination of the OCE technique and the theoretical model presented in this paper provides a framework that can facilitate quantitative viscoelastic characterization of samples with curved geometries and the study of the relationships between morphology and mechanical properties in granular biofilms.


**Keywords:** optical coherence elastography, nondestructive mechanical characterization, viscoelastic properties, circumferential elastic waves, granular biofilms

## 1. Introduction

Granular biofilms are microbial aggregates composed of multispecies bacterial cells and extracellular polymeric substances (EPS) produced by microorganisms. The size of granular biofilms is typically at the millimeter scale[1-4]. In recent years, granular biofilms have generated great interest for wastewater treatment[1, 2]; compared to their predecessor—flocculent activated sludge—that is widely used in wastewater treatment systems, granular biofilms provide several advantages including higher biomass density, stronger cohesiveness, shorter settling time, higher energy efficiency, and less volume required, which leads to a better operational efficiency of wastewater treatment[1-4]. However, despite these beneficial attributes, the number of full-scale municipal or industrial systems utilizing granular biofilms is limited[4, 5]. One reason for their limited use stems from the limited knowledge about the granulation mechanisms that are crucial to controlling the granular biofilms' growth in wastewater treatment systems in a predictable and reproducible fashion[2, 4, 6].

EPS plays an important role in forming the network structure and providing bonding to increase the cohesiveness of microbial aggregates, which ultimately makes the topology of granular biofilms different from flocculent sludge[1-3, 5, 7-10]. The material properties of biofilms are thought to be controlled in part by EPS[11]. EPS contains polymers produced by bacteria such as proteins, polysaccharides, and nucleic acids[2]. Over the last few decades, researchers have investigated the physical properties of EPS[5, 12-16], and these studies suggested that granular biofilms are analogous to hydrogels, particularly in regard to their EPS composition, since they share similar viscoelastic properties. For example, the behavior of EPS is solid-like under small strains as the storage (shear) modulus $G'$ is always larger than the loss modulus $G''$, while under large strains, $G''$ may exceed $G'$ so that the EPS is prone to be liquid-like[5, 12-14]. Rheometry tests also showed that granular biofilms are shear-thinning fluids with yield pseudoplasticity[3, 5, 11-14]. It is worth highlighting that for hydrogels, the gelation phenomenon results from the cross-linking of polymer chains, and the cross-link density is related to the storage modulus $G'$[5, 17]. These discoveries suggest that the viscoelastic behavior of EPS is critical to the granulation of granular biofilms and studying their viscoelastic

properties may further elucidate the key factors required to produce mechanically stable, predictable, and controllable biological aggregates.

Rheometry is a common technique for viscoelastic characterization; however, in the context of granular biofilms, it presents several limitations such as the inability to probe spatially heterogeneous mechanical properties and the inability to conduct measurements with biofilms in their native aqueous solutions. Optical Coherence Elastography (OCE) is a powerful alternative that overcomes these limitations of rheometry[18-20]. OCE has been used for viscoelastic characterization of soft biological materials, particularly in biomedical engineering to evaluate tissue mechanical properties[21-26]. OCE allows for 3D nondestructive imaging of mechanical properties with (1) high spatial resolution at micron-scale, (2) high displacement sensitivity at the nanoscale which minimizes the required magnitude of the external load, preventing large disturbances in the sample, and (3) high sampling rate at $10^1$~$10^2$ kHz that enables real-time monitoring of the sample deformation. Moreover, the OCE image is co-registered with the Optical Coherence Tomography (OCT) image that shows sample's important internal structural features, such as pores in the matrix, which provides a useful tool to study the relationship between the sample morphology and mechanical properties[27].

Recently, a dynamic OCE approach that relies on measurements of elastic wave propagation was shown to be suitable for characterizing the shear modulus and complex shear viscosity of a mixed-culture biofilm with plate-like geometry[28]. While the plate-like biofilm was explored to demonstrate the feasibility of mechanical characterization in environmental biofilms using OCE, broadening application of this technique to granular biofilms is challenging due to their curved geometries and depth-dependent properties that significantly complicate the elastic wave propagation.

In this paper, we report the OCE measurements of elastic wave propagation in a granular biofilm and a theoretical model that is capable of predicting the dispersion (frequency-dependent wave speed) of circumferential elastic waves in a cylindrical viscoelastic solid. The model can approximate the propagation of elastic waves along a circular contour of fixed radius in a spherical sample, and is used for inverse analysis to estimate the viscoelastic properties from OCE measurements of elastic wave propagation. The

inverse analysis approach was validated on alginate spheres with two different concentrations, from which their shear moduli and complex shear viscosities were obtained. We chose alginate as a model system for the OCE measurements because it is commonly present in granular biofilm EPS[7, 11, 15]. The combination of the modeling and experimentation approaches reported in this paper presents a promising framework towards nondestructive characterization of viscoelastic properties in practical environmental biofilms with curved geometries.

## 2. Materials and methods

### 2.1 Sample preparation

Granular biofilms obtained from a full-scale AquaNereda Aerobic Granular Sludge (AGS) Reactor (Aqua-Aerobic Systems, Inc., Rockford, IL, USA) and soft alginate gel samples were characterized with the OCE technique. Spherical alginate (Acros Organics, NJ, USA) samples with 0.8% and 1.2% weight-to-volume (w/v) concentrations were prepared. Mixtures of the two different concentrations were obtained by mixing 0.8 and 1.2 grams of alginate powder, respectively, with a 100 mL solution made from 70 mL of nanopurified water and 30 mL of 5.0% w/v skim milk (Becton, Dickinson and Company 232100, MD, USA). The skim milk was used to increase the optical scattering from the transparent alginate spheres and enhance the OCT image contrast. The alginate solution was stirred in a capped 250 mL Pyrex bottle using a magnetic stir bar with a stir plate (operated at ~400 rpm and heated at 100$^{o}$C) for one hour. Subsequently, the mixture was removed from the stir plate and held at ambient temperature for ~30 minutes to remove entrained air bubbles. Alginate spheres were formed by dripping the mixture into a cross-linking agent made from 25% w/v potassium nitrate and 2% w/v calcium chloride (adapted from Chang and Tseng[29]). The mixture was ejected slowly from a 5 mL pipet tip held horizontally and 10 cm above the surface of the cross-linking agent. Slow ejection speeds were used to ensure that the weight of the droplet was balanced by surface tension, and the droplet hung near the edge of the pipet tip. During the ejection, the size of the droplet increased until a critical volume was reached, and, as the weight exceeded the surface tension, the droplet detached from the pipet tip and fell into the cross-linking agent. The droplet's spherical shape was

formed by surface tension during its free-fall into the cross-linking agent[29]. The spherical droplets solidified in the agent after curing for approximately 30 minutes. OCE experiments were conducted on the cured alginate spheres after 72 hours to ensure that the agent fully diffused through each of them. The process for preparing the alginate spheres is highly repeatable, and the diameter of the spheres falls within the range of 3-5 mm.

**2.2 Experimental setup**

A schematic of the experimental configuration is shown in Fig. 1. The setup was used to generate and monitor elastic wave propagation in the samples. The waves were excited by a paddle actuator in light contact with the sample surface. The actuator was composed of a razor blade, an 18-gauge syringe needle, and a piezoelectric transducer (Thorlabs PZS001, NJ, USA) driven by a radio frequency function generator (Agilent 33120A, CA, USA). The function generator applied a sinusoidal voltage to the transducer to move the needle-blade assembly harmonically along its length, leading to small periodic indentation on the sample surface that generates the harmonic compressional, shear, and circumferential elastic waves. The compressional and shear waves propagate through the interior regions of the sample, and they could be reflected back into the sample or transmitted into the surrounding fluid at the sample boundaries. On the other hand, circumferential waves travel along the curved boundary of the sample, exhibiting frequency-dependent wave speeds and penetration depths. The sample was submerged in water during the experiment to preserve the moisture content and to prevent changes to the material properties (not shown in Fig. 1).

The local displacement induced by the propagating elastic waves was monitored by a phase-sensitive, spectral-domain OCT microscope (Thorlabs GAN210C1). The OCT's imaging mechanism and the method used to synchronize the wave frequency and the scanning rate of the OCT were detailed in our previously published work[28]. The OCT microscope provides two types of image output: (1) the intensity distribution corresponding to the optical scattering from a partially transparent sample due to refractive index variation in the sample (the refractive index variation results from sample's morphology) and (2) the

distribution of the *optical phase difference* $\Delta\phi$ that is related to the local particle displacement in the sample. These two types of images will be referred as OCT and OCE images, respectively, in this paper.

**3. OCE measurements in a granular biofilm**

Figure 2 shows representative OCT and OCE images obtained in a granular biofilm. The sample was submerged in its native aqueous solution from the AGS reactor. The OCT image (Fig. 2a) shows the curved geometry of the granular biofilm. The intensity of the OCT signal decreases with depth from the surface of the biofilm due to attenuation of the probe light, showing that the optical penetration depth is less than 1 mm. Furthermore, the sharp intensity gradient observed near the inner boundary of the biofilm separates the biofilm into an outer bright layer and an inner dark core. The lower signal intensity of the latter is possibly due to the contrasts of the morphology or density in the biofilm[2, 3]. The thickness of the outer layer remains relatively constant (~0.75 mm) within a lateral extent of ~2 mm and reduces monotonically with an abrupt curvature change near the right edge of the OCT image. The OCE image (Fig. 2b) shows the distribution of $\Delta\phi$ that corresponds to the deformation induced by a 2.1 kHz elastic wave confined along the biofilm boundary. The local $\Delta\phi$ signal is proportional to the vertical particle displacement. Note that $\Delta\phi$ is an interferometric parameter that alternates between $-\pi$ to $\pi$ radians, but to enhance visibility of the fringes, the color contour in the OCE image was modified to saturate at the limits $-\pi/2$ and $\pi/2$ radians. The fringes of the $\Delta\phi$ signal within the constant-thickness region yields a wavelength estimate of 1.8 mm (corresponding to the wave speed of 3.78 m/s). It is worth remarking that (1) the apparent wavelength close to the right edge of the biofilm is longer than 1.8 mm due to the change in elastic properties or curvature relative to the left portion of the biofilm, and (2) the elastic wave also interacts with the surrounding fluid, propagating as an interface wave whose amplitude decays with vertical distance into the fluid and the biofilm. Note that in an infinite homogenous elastic solid, the elastic wave speeds of the bulk compressional and shear waves can be directly related to the elastic properties since the wave speeds are frequency- and geometry-independent. However, in the granular biofilm, the elastic wave speed is highly sensitive to the sample heterogeneity, local curvature variation, and the properties of the surrounding fluid. Therefore, to

determine the viscoelastic properties from the OCE data obtained in the granular biofilm, an appropriate inverse modeling approach is needed. The details of the theoretical model developed for this purpose is discussed in the next section.

## 4. Theoretical model

In this section, a theoretical model for calculating the frequency-dependent phase velocity of circumferential elastic waves in a viscoelastic solid with curved geometry is presented. This model was used to quantify the shear modulus and complex shear viscosity of the alginate gel samples though inverse analysis from experimental measurements. To reduce modeling complexity, a two-layer cylindrical geometry illustrated in Fig. 3 was adopted. The inner and outer radii of the cylinder are labeled as $a$ and $b$, respectively. The cylinder is surrounded by an inviscid water half-space ($r > b$) that does not support shear stresses, and all material properties in this structure are homogeneous and isotropic. It has been shown that the waveform supported on the surface of a homogeneous and isotropic sphere is toroidal[30, 31]. The propagation of a toroidal wave can be monitored by probing only on the meridian circle that is normal to the wavefront. As such, the toroidal wave propagation can be approximated by the circumferential wave that travels on the surface of a cylinder with the same curvature of the meridian circle. Therefore, the cylindrical configuration of this model structure is valid and provides a simple approach for modeling the key features of the wave observed in Fig. 2b that is of particular interest to this work: (1) a circumferential wave that travels along a circular contour, and (2) an interface wave (or Sholte wave[32]) that propagates at the interface between the solid and the water.

The elastodynamic wave equation formulated in cylindrical coordinates for harmonic wave propagation in a homogeneous, isotropic, and viscoelastic solid is expressed as[33]

$$(\lambda^* + \mu^*)\nabla(\nabla \cdot \vec{u}) + \mu^* \nabla^2 \vec{u} + \rho\omega^2 \vec{u} = \vec{0} \quad (1)$$

where the displacement vector $\vec{u} = u_r\hat{e}_r + u_\theta\hat{e}_\theta + u_z\hat{e}_z$ comprises the components $u_r$, $u_\theta$, and $u_z$ along $r$-, $\theta$-, and $z$-directions with unit vectors $\hat{e}_r$, $\hat{e}_\theta$, and $\hat{e}_z$; $\rho$ is the density of the material; $\omega$ is the angular frequency; $\nabla$ is the differential operator defined by

$$\nabla = \hat{e}_r\frac{\partial}{\partial r} + \hat{e}_\theta\frac{1}{r}\frac{\partial}{\partial\theta} + \hat{e}_z\frac{\partial}{\partial z}. \quad (2)$$

In eqn (1), $\lambda^*$ and $\mu^*$ are the complex frequency-dependent relaxation functions of the Lamé material properties. Following the Kelvin-Voigt viscoelastic model, the relaxation functions are[32]

$$\lambda^*(\omega) = \lambda + i\eta_\lambda\omega \quad (3)$$

$$\mu^*(\omega) = \mu + i\eta_\mu\omega \quad (4)$$

where $\lambda$ and $\mu$ are the Lamé first parameter and shear modulus, respectively, and $\eta_\lambda$ and $\eta_\mu$ are the corresponding complex viscosities, respectively. The shear modulus $\mu$ and the shear viscosity $\eta_\mu$ are of particular interest in this study.

It can be shown that the solution $\vec{u}$ to eqn (1) is a linear superposition of the contributions from compressional (longitudinal) and shear waves, which can be expressed in terms of a scalar potential $\phi$ and a vector potential $\vec{\psi} = (\psi_r,\psi_\theta,\psi_z)$ by the vector relationship[33]:

$$\vec{u} = \nabla\phi + \nabla\times\vec{\psi} \quad (5)$$

To consider only the plane circumferential interface waves, plane strain conditions are imposed on the displacements and stresses such that (1) the displacement component in the $z$-direction vanishes ($u_z = 0$), and (2) gradients along the $z$-direction are zero ($\partial/\partial z = 0$). From the first condition, the first two components of $\vec{\psi}$ must equal to zero ($\psi_r = \psi_\theta = 0$), yielding $\vec{\psi} = (0,0,\psi)$. From the second condition, the third term of the differential operator in eqn (2) vanishes.

Substituting eqn (5) into eqn (1) leads to the Helmholtz equations for the scalar and vector potentials:

$$\left(\frac{\partial^2}{\partial r^2} + \frac{1}{r}\frac{\partial}{\partial r} + \frac{1}{r^2}\frac{\partial^2}{\partial\theta^2}\right)\phi + \frac{\omega^2}{\alpha_L^2}\phi = 0 \quad (6)$$

$$\left(\frac{\partial^2}{\partial r^2} + \frac{1}{r}\frac{\partial}{\partial r} + \frac{1}{r^2}\frac{\partial^2}{\partial\theta^2}\right)\psi + \frac{\omega^2}{\alpha_S^2}\psi = 0 \quad (7)$$

where $\alpha_L$ and $\alpha_S$ are complex compressional and shear wave speeds that are related to the material properties by the relationships:

$$\alpha_L^2 = \frac{\lambda^* + 2\mu^*}{\rho} \tag{8}$$

$$\alpha_S^2 = \frac{\mu^*}{\rho} \tag{9}$$

The real parts of $\alpha_L$ and $\alpha_S$ are the bulk compressional and shear wave speeds, respectively, and the imaginary parts determine the attenuation (amplitude decay with propagation distance) of the bulk waves.

Following related work in the literature[34, 35], the scalar and vector potential functions corresponding to circumferential interface waves in the solid cylinder are defined as

$$\phi = \Phi(r)e^{i(kb\theta - \omega t)} \tag{10}$$

$$\psi = \Psi(r)e^{i(kb\theta - \omega t)} \tag{11}$$

where $\Phi(r)$ and $\Psi(r)$ represent the complex amplitudes along the radial ($r$) direction; $k$ is the complex wavenumber whose real part $\mathrm{Re}\{k\} = k^R$ is related to the wavelength $\lambda$ by $k^R = 2\pi/\lambda$ and imaginary part represents the wave attenuation.

From eqn (6), (7), (10) and (11), we obtain the following differential equations that $\Phi(r)$ and $\Psi(r)$ must satisfy:

$$\frac{d^2\Phi}{dr^2} + \frac{1}{r}\frac{d\Phi}{dr} + \left(k_L^2 - \frac{k^2b^2}{r^2}\right)\Phi = 0 \tag{12}$$

$$\frac{d^2\Psi}{dr^2} + \frac{1}{r}\frac{d\Psi}{dr} + \left(k_S^2 - \frac{k^2b^2}{r^2}\right)\Psi = 0 \tag{13}$$

where $k_L = \omega/\alpha_L$ and $k_S = \omega/\alpha_S$ are complex wavenumbers for the bulk compressional and shear waves.

Eqn (12) and (13) are Bessel differential equations whose general solutions are linear superpositions of Bessel functions as expressed below:

$$\Phi(r) = A_1 J_\nu(k_L r) + A_2 Y_\nu(k_L r) \tag{14}$$

$$\Psi(r) = A_3 J_\nu(k_S r) + A_4 Y_\nu(k_S r) \tag{15}$$

where $A_1$, $A_2$, $A_3$, and $A_4$ are unknown coefficients, $J_\nu(x)$ and $Y_\nu(x)$ are Bessel functions of the first and second kind, and $\nu = kb$ is the order of the Bessel functions.

In cylindrical coordinates, the components of the particle displacement and the stress tensor have the relationships with the scalar and vector potentials as below:

$$u_r = \frac{\partial \phi}{\partial r} + \frac{1}{r}\frac{\partial \psi}{\partial \theta} \tag{16}$$

$$u_\theta = \frac{1}{r}\frac{\partial \phi}{\partial \theta} - \frac{\partial \psi}{\partial r} \tag{17}$$

$$\sigma_{rr} = (\lambda^* + 2\mu^*)\frac{\partial^2 \phi}{\partial r^2} + \lambda^*\left(\frac{1}{r}\frac{\partial \phi}{\partial r} + \frac{1}{r^2}\frac{\partial^2 \phi}{\partial \theta^2}\right) + 2\mu^*\left(\frac{1}{r}\frac{\partial^2 \psi}{\partial r \partial \theta} - \frac{1}{r^2}\frac{\partial \psi}{\partial \theta}\right) \tag{18}$$

$$\sigma_{r\theta} = \mu^*\left(\frac{2}{r}\frac{\partial^2 \phi}{\partial r \partial \theta} - \frac{2}{r^2}\frac{\partial \phi}{\partial \theta} - \frac{\partial^2 \psi}{\partial r^2} + \frac{1}{r}\frac{\partial \psi}{\partial r} + \frac{1}{r^2}\frac{\partial^2 \psi}{\partial \theta^2}\right) \tag{19}$$

By substituting eqn (10) and (11) into eqn (16) – (19), using the expressions for $\Phi(r)$ and $\Psi(r)$ in eqn (14) and (15), the components of the particle displacement and the stress tensor can be expressed in terms of the unknown coefficients and combined as the following matrix set:

$$\begin{bmatrix} u_r \\ u_\theta \\ \sigma_{rr} \\ \sigma_{r\theta} \end{bmatrix} = \begin{bmatrix} D_{11} & D_{12} & D_{13} & D_{14} \\ D_{21} & D_{22} & D_{23} & D_{24} \\ D_{31} & D_{32} & D_{33} & D_{34} \\ D_{41} & D_{42} & D_{43} & D_{44} \end{bmatrix} \begin{bmatrix} A_1 \\ A_2 \\ A_3 \\ A_4 \end{bmatrix} e^{i(kb\theta - \omega t)} \tag{20}$$

The expressions of the matrix elements $D_{mn}$ ($m$,$n$ = 1,2,3,4) in eqn (20) are provided in the Appendix.

The displacement and pressure in the surrounding water half-space are formulated in terms of a scalar potential function $\phi^w$. The displacement is given by the gradient of $\phi^w$:

$$\overrightarrow{u^w} = \nabla \phi^w \tag{21}$$

Eqn (21) does not include the vector potential because the water half-space is assumed to be inviscid and does not support shear waves.

We specifically focused on the solution of the interface waves that are simultaneously coupled in the solid and the water half-space. We formulated this by matching the phase of the scalar potential in the water to that in the solid, such as

$$\phi^w = \Phi^w(r) e^{i(kb\theta - \omega t)} \tag{22}$$

where the complex amplitude $\Phi^w(r)$ must satisfy the Bessel differential equation

$$\frac{d^2\Phi^w}{dr^2} + \frac{1}{r}\frac{d\Phi^w}{dr} + \left(k_w^2 - \frac{k^2 b^2}{r^2}\right)\Phi^w = 0 \tag{23}$$

that is obtained by substituting eqn (22) into eqn (6). In eqn (23), $k_w = \omega/\alpha_L^w$ is the wavenumber of the compressional wave as $\alpha_L^w =$ 1481 m/s is the wave speed in water. Because the water half-space is assumed to be inviscid, $\alpha_L^w$ is a real number without the imaginary part. Moreover, the water half-space has no excitation source, as such, only the partial waves traveling outward in the radial direction exist in the water, and the solution of eqn (23) is represented by the Hankel function of the first kind, given by

$$\Phi^w(r) = A_5 H_\nu^{(1)}(k_w r) \tag{24}$$

The unknown coefficient $A_5$ is determined by the boundary conditions at the solid-water interface.

From eqn (16), (18), and (21) − (24), the displacement and the pressure (equivalent to the normal stresses in the solid) along the radial direction in the water half-space are derived as functions of the unknown coefficient $A_5$:

$$u_r^w = \left(k_w H_\nu^{(1)\prime}\right) A_5 e^{i(kb\theta - \omega t)} \tag{25}$$

$$p = \left(\lambda^w k_w^2 H_\nu^{(1)\prime\prime} + \lambda^w \frac{1}{r} k_w H_\nu^{(1)\prime} - \lambda^w \frac{\nu^2}{r^2} H_\nu^{(1)}\right) A_5 e^{i(kb\theta - \omega t)} = P(r) A_5 e^{i(kb\theta - \omega t)} \tag{26}$$

where

$$H_\nu^{(1)} = H_\nu^{(1)}(k_w r),\ H_\nu^{(1)\prime} = \frac{d}{d(k_w r)}\left(H_\nu^{(1)}(k_w r)\right),\ H_\nu^{(1)\prime\prime} = \frac{d^2}{d(k_w r)^2}\left(H_\nu^{(1)}(k_w r)\right) \tag{27}$$

In eqn (26), $\lambda^w$ is the Lamé first parameter for the water half-space that is related to the compressional wave speed $\alpha_L^w$ and the water density $\rho^w$ by $\lambda^w = \rho^w\left(\alpha_L^w\right)^2$.

To determine the five unknown coefficients associated with the potential functions in the solid and water, five boundary conditions are required. Here, we prescribe the inner boundary (r = a) to be rigid, so the boundary conditions are (1) continuity of the displacement along radial direction at the water-sphere interface, $u_r|_{r=b} = u_r^w|_{r=b}$, (2) continuity of the normal traction in the solid and pressure in the water at the water-solid interface, $\sigma_{rr}|_{r=b} = p|_{r=b}$, (3) zero shear traction at the water-solid interface, $\sigma_{r\theta}|_{r=b} = 0$, (4) zero radial displacement at the inner boundary, $u_r|_{r=a} = 0$, and (5) zero circumferential displacement at the inner boundary, $u_\theta|_{r=a} = 0$. Applying these boundary conditions leads to five equations for the coefficients as shown in the matrix form below:

$$\begin{bmatrix} D_{11}|_{r=b} & D_{12}|_{r=b} & D_{13}|_{r=b} & D_{14}|_{r=b} & -k_w H_\nu^{(1)\prime}|_{r=b} \\ D_{31}|_{r=b} & D_{32}|_{r=b} & D_{33}|_{r=b} & D_{34}|_{r=b} & -P(r)|_{r=b} \\ D_{41}|_{r=b} & D_{42}|_{r=b} & D_{43}|_{r=b} & D_{44}|_{r=b} & 0 \\ D_{11}|_{r=a} & D_{12}|_{r=a} & D_{13}|_{r=a} & D_{14}|_{r=a} & 0 \\ D_{21}|_{r=a} & D_{22}|_{r=a} & D_{23}|_{r=a} & D_{24}|_{r=a} & 0 \end{bmatrix} \begin{bmatrix} A_1 \\ A_2 \\ A_3 \\ A_4 \\ A_5 \end{bmatrix} = \mathbf{0}$$

or

$$\mathbf{SA} = \mathbf{0} \tag{28}$$

To obtain non-trivial solutions for unknown coefficients in matrix **A** of eqn (28), the determinant of the matrix **S** must equal to zero[36]:

$$\det(\mathbf{S}) = 0 \tag{29}$$

which is the characteristic equation of this model. Solving the characteristic equation yields infinite solution pairs of angular frequency and complex wavenumber ($\omega$,$k$) that represent the dispersion relation of the plane circumferential interface wave in the water-loaded cylindrical solid. The phase velocity ($c$) of the interface wave is obtained from the relation between the angular frequency $\omega$ and the real part of the complex wavenumber $\mathrm{Re}\{k\} = k^R$, defined by $c = \omega/k^R$. Since the matrix **S** is complex, eqn (29) is solved by searching the combinations of ($\omega$,$k$) where the determinant of **S** has zero magnitude, |det(**S**)| = 0. Note that it may be difficult to achieve absolute zero in numerical calculation; therefore, in practice, the solutions are determined instead by locating local minima in the ($\omega$,$k$) space. (see Section S1 of the Supplementary Information for further details).

## 5. Results and discussion

### 5.1 Numerical simulation

The theoretical model presented in the previous section was implemented numerically in a commercial software MATLAB (Release R2016b, MathWorks) to calculate the dispersion curves for the circumferential elastic waves. The model was validated against a thin, pure-elastic curved plate with a very small thickness to inner radius ratio $(b - a)/a = 0.05$, which approximates the *curved* plate to a *flat* plate. The plate has the same parameters and boundary conditions as those reported by Liu and Qu (1998)[34]: $a$ =

20 mm, $b = a/0.95$, $\alpha_L$ = 5660 m/s, $\alpha_S$ = 3200 m/s, and traction-free boundary conditions at the inner and outer boundaries ($r = a$ and $b$). The characteristic equation for this case is discussed in Section S2 of Supplementary Information. The dispersion curves for the thin curved plate were calculated by our MATLAB program, and the results are presented in Fig. 4 by plotting the normalized angular frequency $\overline{\omega} = \omega(b-a)/\alpha_S$ against the normalized wavenumber $\overline{k} = k(b-a)$, which is the same as the Fig. 2(c) in Liu and Qu (1998).

From Fig. 4, we observe that the dispersion curves for the thin *curved* plate resemble the antisymmetric and symmetric guided wave modes in a thin *flat* plate—(1) the phase velocities of the two lowest modes are strongly frequency-dependent at low frequencies, but become non-dispersive at high frequencies, approaching the Rayleigh wave velocity; (2) the higher order modes originate at cut-off frequencies defined by $\overline{\omega}_c = (\alpha_L/\alpha_S)n\pi$ or $\overline{\omega}_c = n\pi$ ($n$ = 1,2,3,…) for longitudinal or shear thickness resonance modes, respectively. These resemblances, which are expected due to the flatness of the thin curved plate, provide the validation for the circumferential elastic wave model. In addition, the dispersion curves shown in Fig. 4 are identical to those calculated by Liu and Qu (1998), which verifies the correctness of our MATLAB program. Note that the axis parameters for Fig. 4 were chosen to be the same as those used by Liu and Qu[34] for easy and direct comparison. For the other dispersion curves presented in this paper, the phase velocity was plotted as a function of frequency. The dispersion curve of phase velocity is directly relevant to the OCE measurements and will be used for inverse analysis to quantify the viscoelastic properties.

Next, the dispersion curve for the lowest order mode is examined to understand the penetration depth of the circumferential interface wave and how its phase velocity is affected by the viscoelastic properties and the outer boundary curvature of the water-loaded model cylinder. The model material was assumed to be homogeneous, isotropic biofilm with the density $\rho$ = 1000 kg/m$^3$, longitudinal wave speed $\alpha_L$ = 1481 m/s, and shear wave speed $\alpha_S$ = 2 m/s. $\rho$ and $\alpha_L$ were chosen to be the same as water due to the

high ratio of water content (over 90%) in biofilms[28]. The boundary condition of the inner boundary ($r = a$) was assumed to be rigid.

The penetration depth of the circumferential elastic wave is investigated by fixing the outer radius $b$ = 2 mm and changing the inner radius $a$ of the cylinder. Figure 5a shows a series of dispersion curves for three different inner radii $a$ = 0.1 μm, 0.5 mm and 1 mm. The dispersion curves are plotted with the phase velocity $c$ and frequency $f$ on the ordinate and abscissa axes, respectively, for convenience. All dispersion curves originate from higher phase velocities at low frequency region and decrease monotonically with frequency. The difference at low frequencies results from the cut-off frequencies of the modes for these cases since the cut-off frequency increases with reduced thickness. The overall decreasing trends of the dispersion curves imply that the penetration depths, which have positive correlation with the wavelengths $\Lambda$ (determined by $\Lambda = c/f$), also decrease with frequency for these three cases. Take the case $a$ = 1 mm for example, below 2700 Hz, the dispersion curve has higher phase velocity than other two cases since the penetration depth is still larger or comparable to the thickness between the two boundaries ($b - a$ = 1 mm) so that the wave propagates as a guided wave that interacts with both boundaries of the cylinder. Above 2700 Hz, the penetration depth becomes smaller than all three thicknesses considered so that three dispersion curves collapse on top of each other, indicating the wave propagates as an interface wave whose energy is confined near the solid-water interface. At the transition frequency 2700 Hz, we may conclude that the penetration depth of the interface wave is 1 mm, while the wavelength, calculated from the phase velocity 2.75 m/s, is 1.02 mm, which confirms the common rule-of-thumb that the penetration depth of the interface wave is approximately equal to one wavelength. This attribute of the interface wave may be suitable for depth profiling of the viscoelastic properties in a radially gradient sample through measurements of the frequency-dependent wave speeds.

The calculated dispersion curves for water-loaded pure-elastic and viscoelastic cylinders are compared in Fig. 5b. For these calculations, the complex viscosity was changed from $\eta_\mu = 0$ for the pure-elastic case to $\eta_\mu$ = 0.1 Pa-s for the viscoelastic case. The inner and outer radii of the cylinder are $a$ = 0.1 μm and $b$ = 2 mm. For the pure-elastic cylinder, the phase velocity of the interface wave decreases

monotonically with frequency. On the other hand, the viscoelastic cylinder has similar decreasing phase velocity at low frequencies but shows a flattened trend from 2500 Hz and a slight increase beyond 3500 Hz. This is because the complex shear modulus of the viscoelastic cylinder increases linearly with frequency by the factor of the shear viscosity as defined in eqn (4). The increase in the phase velocity of the interface wave at high frequencies is directly related to the viscoelastic properties of the material and will be explored in this paper to characterize the complex shear modulus of the curved alginate gel samples.

Finally, the influence of the radius of curvature on the phase velocity of the interface wave in the water-loaded viscoelastic cylinder is presented in Fig. 5c. Three different outer radii ($b$ = 1.5 mm, 2 mm, 2.5 mm) were used in the calculations, while the inner radius was fixed to $a$ = 0.1 μm. The shear viscosity is the same as the viscoelastic case in Fig. 5b ($\eta_\mu$ = 0.1 Pa-s). The dispersion curves in Fig. 5c show a clear dependence of the phase velocity on the radius of curvature of the solid-water interface—the phase velocity decreases with the radius of curvature. In addition, all dispersion curves show the flattened-to-increase trends at high frequencies, which results from the escalating complex shear modulus with frequency by the factor of shear viscosity as observed in Fig. 5b. The results suggest that the curvature of the interface plays an important role in the frequency-dependent phase velocity of the interface wave. We will accommodate the curvature effect in the analysis works in following sections.

**5.2 Application of OCE and model-based inverse analysis to alginate gel spheres**

Figure 6 shows representative OCT and OCE images for a 0.8% alginate sphere with a diameter of 4 mm submerged in water. During the experiments, the water height was kept at least 2 mm higher than the top of the sphere, so that the effect of the water surface on the circumferential interface waves was negligible. The OCT image shows very limited intensity variation within the sample, indicating structural homogeneity and the integrity (no voids or cracks) of the sample. The local intensity in the OCT image decreases with depth below the sample surface due to attenuation of the OCT light source. The penetration depth of the OCT light beam depends on the wavelength of light source and the optical properties of the sample. The OCE image shows periodic oscillation of the optical phase difference $\Delta\phi$ associated with the periodic

displacement profile of the elastic wave excited by the actuator at 1600 Hz. The displacement profile follows the curvature of the sample surface, as expected for a circumferential interface wave. The amplitude of the fringes decreases with the circumferential distance from the source due to damping in the viscoelastic solid.

To determine the phase velocity of the circumferential wave, which equals to the product of the excitation frequency and the wavelength, the wavelength was obtained from the fringes in the OCE image by following four steps: (1) the contour of the sample surface in the OCT image was identified; (2) a circular arc was fitted to the contour to determine the approximate radius of curvature and the propagation path (white dotted line in Fig. 6b); (3) the spatial OCE data along the propagation path was processed by fast Fourier transform to obtain the amplitude spectrum from which the spatial frequency ($1/\overline{\Lambda}$, $\overline{\Lambda}$ is the wavelength) of the wave was determined. For convenience, the curve fitting in step (2) was performed in the cylindrical ($r$-$\theta$) coordinates system instead of the normal Cartesian ($x$-$y$) system so that the wavelength $\overline{\Lambda}$ has the unit of radians rather than meters, and the phase velocity of the interface wave $c$ was calculated using the relationship $c = fb\overline{\Lambda}$ where $f$ is the excitation frequency and $b$ is the radius of curvature.

The measurements of the frequency-dependent elastic wave speed were conducted on alginate spheres with 0.8% and 1.2% alginate concentration. For each concentration, the measurements were repeated on three samples of similar sizes. The experimental results of the six samples are demonstrated by the sparse circles in Fig. 7. Comparing the overall ranges of the experimentally measured wave speeds from the 0.8% and 1.2% alginate spheres, as expected, the results from the 1.2% alginate spheres have higher wave speeds. In addition, all examples show that wave speeds slightly increase or remain relatively constant with increasing frequency. This suggests that the dispersion curves are clearly different from the elastic case, where the phase velocity decreases with frequency, as shown in Fig. 5b; therefore, the shear viscosity needs to be considered when employing the theoretical model to predict the dispersion curves and obtain the best fits for the experimental data.

The best-fit dispersion curves are presented by the solid lines in Fig. 7, which show good agreement with the experimental data. The curves were calculated by using the shear modulus and the complex shear

viscosity as free fitting parameters in the numerical model. The best-fit viscoelastic properties and other parameters used for calculating the dispersion curves are listed in Table 1. The average shear moduli and complex shear viscosities from the measurements on samples with the same concentration are shown in Fig. 8a and 8b, respectively. For every data point in Fig. 8, the circular marker indicates the average over three samples, and the error bar represents the standard deviation. The coefficient of variation (COV), defined by the ratio of the standard deviation to the average value, of each data point is presented in Table 2. The COV values imply small variabilities of shear moduli and complex shear viscosities from sample to sample with the same alginate concentration, and the stronger sensitivity of the dispersion curves to the shear modulus versus the complex shear viscosity. We remark that the shear moduli are in the same order of magnitude with the ones characterized with rheometry[5, 37]. Furthermore, the shear moduli and the complex shear viscosities of the 0.8% samples are within the same order of magnitude of those found in a mixed-culture biofilm as reported in our previous work[28], which verifies a commonly accepted analogy between the alginate and bacterial biofilms in terms of mechanical properties.

The calculations for alginate spheres in Fig. 7 were carried out by using a small value for the inner radius $a$ to eliminate the effect from the inner boundary. This inevitably leads to a limitation that the energy carried by the circumferential interface waves must be distributed within the span $[a,b]$. As such, the model is unable to capture low frequency interface waves that have penetration depths longer than or comparable to the radius of the sphere. On the other hand, for high frequency interface waves, this limitation does not hinder the accuracy of the frequency-dependent phase velocity since the penetration depths of the waves at high frequencies are short so that the effect from the inner boundary is negligible. Therefore, the frequency range 1.6~4 kHz was selected for experimental measurements to limit the penetration depths. For example, the wave speed at 1.6 kHz in Fig. 7e is 3.11 m/s and the corresponding wavelength is 1.94 mm, which is smaller than the sphere radius. In addition, this frequency range provides (1) good signal-to-noise ratio of the OCE images, which deteriorates with frequency due to wave attenuation; (2) sufficient alternating fringes of displacement profile in the OCE images to enhance the estimate accuracy of the circumferential wavelength and the corresponding wave speed. A minimum of three fringe cycles is required to achieve the

estimate precision of 0.02 m/s. In the example of Fig. 7e mentioned above, the circumference length of ~7 mm contains more than three spatial periods of the circumferential wave at 1.6 kHz, which is beyond the requirement of fringe number to reach desired estimate accuracy.

The frequency bandwidth of Kelvin-Voigt model $f_{bw}$ to characterize material's viscoelasticity is controlled by the retardation time of the material, defined by $f_{bw} = 1/t_R = \mu/\eta_\mu$. By substituting the characterization results in Table 1 into this relation, the applicable bandwidths for 0.8% and 1.2% alginate gel samples are 28 and 22 kHz, respectively. Since the frequency range used in the OCE measurements was much lower than the bandwidths, it is valid to apply the Kelvin-Voigt model for the viscoelasticity characterization of the alginate samples.

The framework developed here—combining the OCE measurements of circumferential interface waves and the model-based inverse analysis—paves the way for the mechanical characterization of real granular biofilms utilized in wastewater treatment systems. The structure of the theoretical model (the boundaries at $r = a$ and $b$) allows for extending to the layered granular biofilm (Fig. 2a), where the frequency-dependent circumferential interface wave can be harnessed to its compositional distribution. The knowledge gained from this study can advance our understanding of structure-composition-mechanical properties relationship in granular biofilms and to enhance their performance in wastewater treatment reactors.

## 6. Conclusions

In this paper, we first demonstrated the feasibility of OCE measurements in real granular biofilms obtained from a wastewater treatment facility, and then developed a metrology approach that combines the OCE measurements with a forward modeling of the dispersion relation of circumferential interface waves in soft viscoelastic samples with curved geometries. The OCE technique was used to obtain the geometry- and frequency-dependent phase velocities of the circumferential interface wave propagating in alginate spheres surrounded by water. The numerical model was based on the elastodynamic wave equation, from which the frequency-dependent phase velocities of elastic waves in a water-loaded curved sample were predicted

using the information of sample geometry, material properties, and the boundary conditions. Our numerical calculations suggest that the circumferential interface wave is highly dependent on sample geometry and composition. The numerical model was fitted to the OCE data to estimate the shear moduli and complex shear viscosities of the alginate spheres. This framework was used to characterize the shear moduli and complex shear viscosities of alginate spheres with two different concentrations (0.8% and 1.2% w/v). The estimated properties are in good agreement with reported values in the literature. Our future work will aim at mapping depth-dependent structural differences in granular biofilms by representative layering in the theoretical model. Ultimately, this effort can facilitate deeper understanding of the relationship between morphology, biological and chemical composition, and spatially heterogeneous mechanical properties in granular biofilms. Furthermore, the numerical model can be used to study elastic wave propagation in curved structures from other areas. For example, the approach we describe based on circumferential elastic waves may find application in viscoelastic characterization of cornea and may be of use as a predictive tool for evaluating ophthalmic disease state.

**Conflicts of interest**

The authors declare no conflicts of interest.

**Acknowledgements**

We wish to thank Aqua-Aerobic Systems, Inc. (Rockford, IL, USA) for providing granular biofilms for this work. The authors also acknowledge the support of the National Science Foundation via Award CBET-1701105, and the Civil and Environmental Engineering Department at Northwestern University for providing seed funding for this project.

**Appendix: D Matrix**

Details of the elements $D_{mn}$ in eqn (20):

$$D_{11} = k_L J_\nu^{L\prime} \tag{A1}$$

$$D_{12} = k_L Y_\nu^{L\prime} \tag{A2}$$

$$D_{13} = i\frac{\nu}{r} J_\nu^S \tag{A3}$$

$$D_{14} = i\frac{\nu}{r} Y_\nu^S \tag{A4}$$

$$D_{21} = i\frac{\nu}{r} J_\nu^L \tag{A5}$$

$$D_{22} = i\frac{\nu}{r} Y_\nu^L \tag{A6}$$

$$D_{23} = -k_S J_\nu^{S\prime} \tag{A7}$$

$$D_{24} = -k_S Y_\nu^{S\prime} \tag{A8}$$

$$D_{31} = (\lambda^* + 2\mu^*) k_L^2 J_\nu^{L\prime\prime} + \lambda^* \frac{1}{r} k_L J_\nu^{L\prime} - \lambda^* \frac{\nu^2}{r^2} J_\nu^L \tag{A9}$$

$$D_{32} = (\lambda^* + 2\mu^*) k_L^2 Y_\nu^{L\prime\prime} + \lambda^* \frac{1}{r} k_L Y_\nu^{L\prime} - \lambda^* \frac{\nu^2}{r^2} Y_\nu^L \tag{A10}$$

$$D_{33} = 2i\mu^* \frac{\nu}{r} k_S J_\nu^{S\prime} - 2i\mu^* \frac{\nu}{r^2} J_\nu^S \tag{A11}$$

$$D_{34} = 2i\mu^* \frac{\nu}{r} k_S Y_\nu^{S\prime} - 2i\mu^* \frac{\nu}{r^2} Y_\nu^S \tag{A12}$$

$$D_{41} = 2i\mu^* \frac{\nu}{r} k_L J_\nu^{L\prime} - 2i\mu^* \frac{\nu}{r^2} J_\nu^L \tag{A13}$$

$$D_{42} = 2i\mu^* \frac{\nu}{r} k_L Y_\nu^{L\prime} - 2i\mu^* \frac{\nu}{r^2} Y_\nu^L \tag{A14}$$

$$D_{43} = -\mu^* k_S^2 J_\nu^{S\prime\prime} + \mu^* \frac{1}{r} k_S J_\nu^{S\prime} - \mu^* \frac{\nu^2}{r^2} J_\nu^S \tag{A15}$$

$$D_{44} = -\mu^* k_S^2 Y_\nu^{S\prime\prime} + \mu^* \frac{1}{r} k_S Y_\nu^{S\prime} - \mu^* \frac{\nu^2}{r^2} Y_\nu^S \tag{A16}$$

as

$$B_\nu^\beta = B_\nu(k_\beta r),\ B = J \text{ or } Y,\ \beta = L \text{ or } S \tag{A17}$$

and

$$B_\nu^{\beta\prime} = \frac{d}{d(k_\beta r)}(B_\nu(k_\beta r)),\ B_\nu^{\beta\prime\prime} = \frac{d^2}{d(k_\beta r)^2}(B_\nu(k_\beta r)) \tag{A18}$$

**References**


1. K. Milferstedt, J. Hamelin, C. Park, J. Jung, Y. Hwang, S.-K. Cho, K.-W. Jung, and D.-H. Kim, *Int. J. Hydrog. Energy*, 2017, **42**, 27801-27811.
2. S. J. Sarma, J. H. Tay, and A. Chu, *Trends Biotechnol.*, 2017, **35**, 66-78.
3. X. Liu, G. Sheng, and H. Yu, *Biotechnol. Adv.*, 2009, **27**, 1061-1070.
4. Y. Liu, and J.-H. Tay, *Water Res.*, 2002, **36**, 1653-1665.
5. T. Seviour, M. Pijuan, T. Nicholson, J. Keller, and Z. Yuan, *Biotechnol. Bioeng.*, 2009, **102**, 1483-1493.
6. Q. Zhang, J. Hu, and D. Lee, *Bioresour. Technol.*, 2016, **201**, 74-80.
7. S. S. Adav, D.-J. Lee, and J.-H. Tay, *Water Res.*, 2008, **41**, 1644-1650.
8. C. Caudan, A. Filali, M. Spérandio, and E. Girbal-Neuhauser, *Chemosphere*, 2014, **117**, 262-270.
9. Z. Ding, I. Bourven, G. Guibaud, E. D. van Hullebusch, A. Panico, F. Pirozzi, and G. Esposito, *Appl. Microbiol. Biotechnol.*, 2015, **99**, 9883-9905.
10. L. Zhu, M. Lv, X. Dai, Y. Yu, H. Qi, and X. Xu, *Bioresour. Technol.*, 2012, **107**, 46-54.
11. S. Felz, S. Al-Zuhairy, O. A. Aarstad, M. C. van Loosdrecht, and Y. M. Lin, *J. Vis. Exp*., 2016, **115**, 54534.
12. H.-F. Wang, H. Hu, H.-Y. Yang, and R. J. Zeng, *Water Res.*, 2016, **106**, 116-125.
13. X. Lin and Y. Wang, *Water Res.*, 2017, **120**, 22-31.
14. Y.-J. Ma, C.-W. Xia, H.-Y. Yang, and R. J. Zeng, *Water Res.*, 2014, **50**, 171-178.
15. Y. M. Lin, P. K. Sharma, M. C. M. van Loosdrecht, *Water Res.*, 2013, **47**, 57-65.
16. T. Seviour, M. Pijuan, T. Nicholson, J. Keller, and Z. Yuan, *Water Res.*, 2009, **43**, 4469-4478.
17. V. Sekkar, K. Narayanaswamy, K. J. Scariah, P. R. Nair, K. S. Sastri, and H. G. Ang, *J. Appl. Polym. Sci.*, 2007, **103**, 3129–3133.
18. X. Liang, V. Crecea, and S. A. Boppart, *J. Innov. Opt. Health Sci.*, 2010, **3**, 221–233.
19. B. F. Kennedy, K. M. Kennedy, and D. D. Sampson, *IEEE J. Sel. Top. Quantum Electron.*, 2014, **20**, 7101217.
20. M. Wagner and H. Horn, *Biotechnol. Bioeng.*, 2017, **114**, 1386-1402.
21. K. V. Larin and D. D. Sampson, *Biomed. Opt. Express*, 2017, **8**, 1172-1202.
22. S. Wang and K. V. Larin, *J. Biophotonics*, 2015, **8**, 279–302.
23. Ł. Ambroziński, S. Song, S. J. Yoon, I. Pelivanov, D. Li, L. Gao, T. T. Shen, R. K. Wang, and M. O'Donnell, *Sci. Rep.*, 2016, **6**, 38967.
24. S. Song, Z. Huang, T.-M. Nguyen, E. Y. Wong, B. Arnal, M. O'Donnell, and R. K. Wang, *J. Biomed. Opt.*, 2013, **18**, 121509.
25. V. Crecea, A. Ahmad, and S. A. Boppart, *J. Biomed. Opt.*, 2013, **18**, 121504.

26. M. A. Kirby, I. Pelivanov, S. Song, Ł. Ambrozinski, S. J. Yoon, L. Gao, D. Li, T. T. Shen, R. K. Wang, and M. O'Donnell, *J. Biomed. Opt.*, 2017, **22**, 121720.
27. A. F. Rosenthal, J. S. Griffin, M. Wagner, A. I. Packman, O. Balogun, and G. F. Wells, *Biotechnol. Bioeng.*, 2018, **115**, 2268-2279.
28. H.-C. Liou, F. Sabba, A. I. Packman, G. Wells, and O. Balogun, *Soft Matter*, 2019, **15**, 575-586.
29. C. C. Chang and S. K. Tseng, *Biotechnology Techniques*, 1998, **12**, 865-868.
30. S. Towfighi and T. Kundu, *Int. J. Solids Struct*. 2003, **40**, 5495–5510.
31. J. Yu, B. Wu, H. Huo, and C. He, *Wave Motion*, 2007, **44**, 271–281.
32. J. L. Rose, *Ultrasonic Waves in Solid Media*, 1999.
33. J. D. Achenbach, *Wave Propagation in Elastic Solids*, 1973, 79-121.
34. G. Liu and J. Qu, *J. Appl. Mech.*, 1998, **65**, 424-430.
35. K. L. J. Fong, *A Study of Curvature Effects on Guided Elastic Waves*, 2005, Ph. D. Thesis, Imperial College London.
36. M. J. S. Lowe, *IEEE Trans. Ultrason. Ferroelectr. Freq. Control*, 1995, **42**, 525-542.
37. M. A. LeRoux, F. Guilak, and L. A. Setton, *J. Biomed. Mater. Res*., 1999, **47**, 46-53.

# Figures and Tables

# Towards Mechanical Characterization of Granular Biofilms by Optical Coherence Elastography Measurements of Circumferential Elastic Waves

*Hong-Cin Liou[1], Fabrizio Sabba[2], Aaron I. Packman[2], Alex Rosenthal[2], George Wells[2], Oluwaseyi Balogun[1,2*]*

[1]Mechanical Engineering Department, Northwestern University, Evanston, IL 60208

[2]Civil and Environmental Engineering Department, Northwestern University, Evanston, IL 60208

***Corresponding author:**

Oluwaseyi Balogun, Phone: +1 847-491-3054; e-mail: o-balogun@u.northwestern.edu

**The following are included as figures for this paper:**

Number of pages: 13

Number of figures: 8

Number of tables: 2

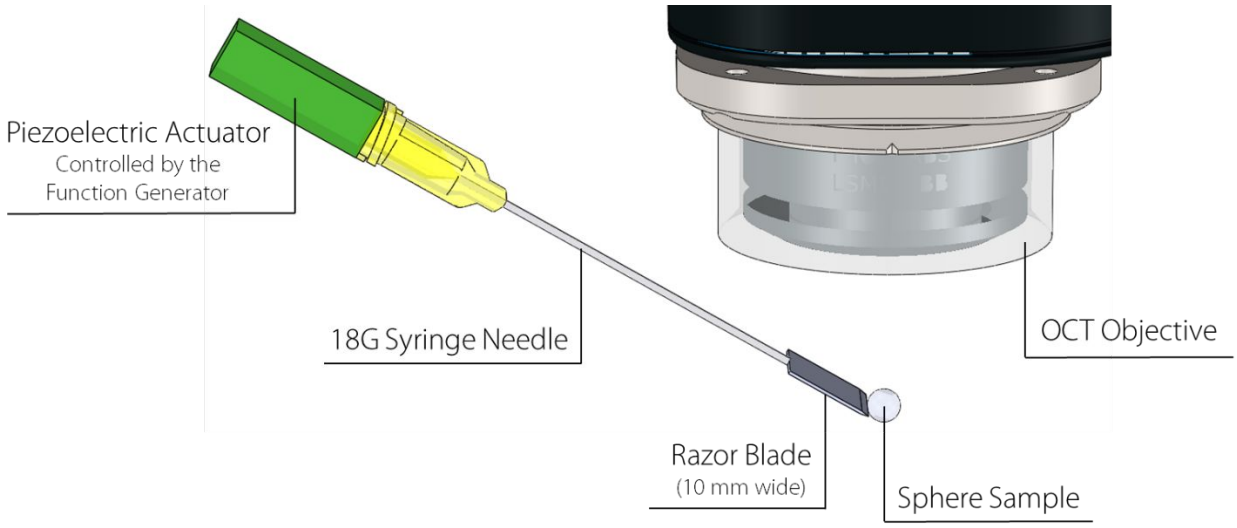


**Fig. 1.** Optical coherence elastography setup.

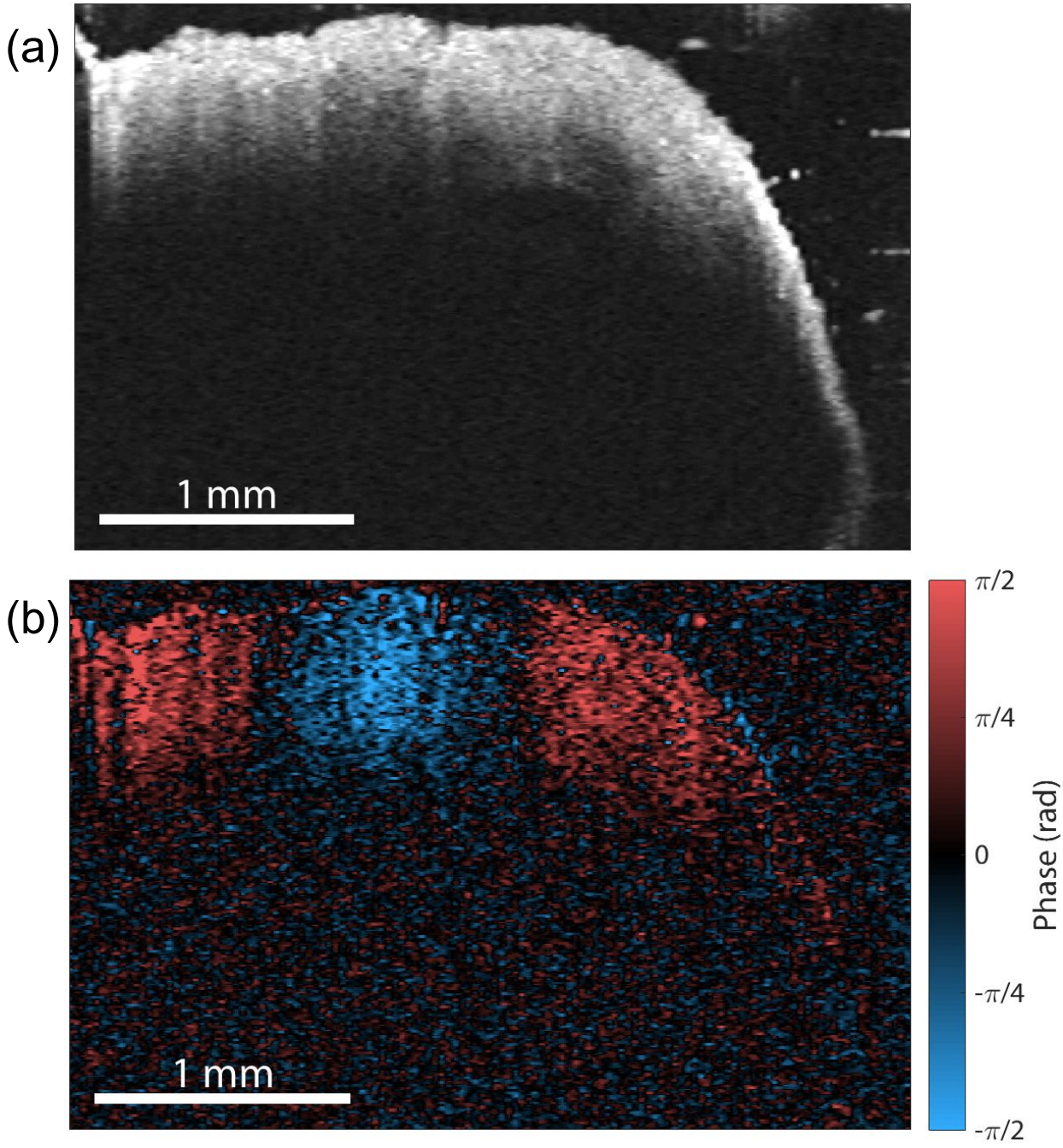


**Fig. 2.** (a) OCT image and (b) OCE image of the granular biofilm (excitation frequency 2.1 kHz).

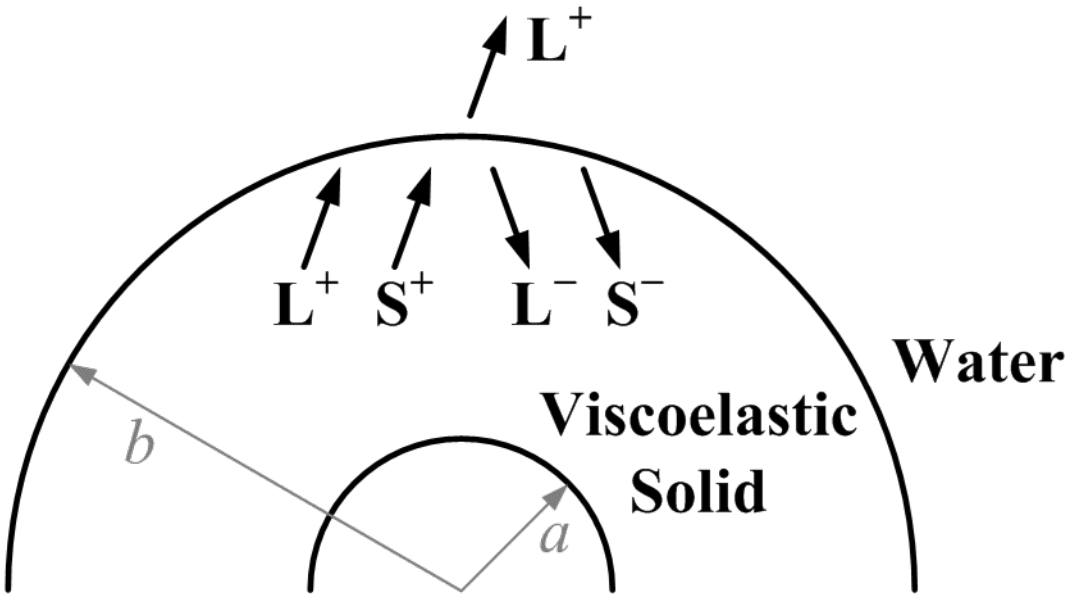


**Fig. 3.** Geometry of the multilayered model cylinder for circumferential elastic waves. Symbols L and S represent longitudinal and shear waves. Positive and negative superscripts represent outward and inward propagating partial waves. *a* and *b* are the inner and outer radii of the viscoelastic solid layer.

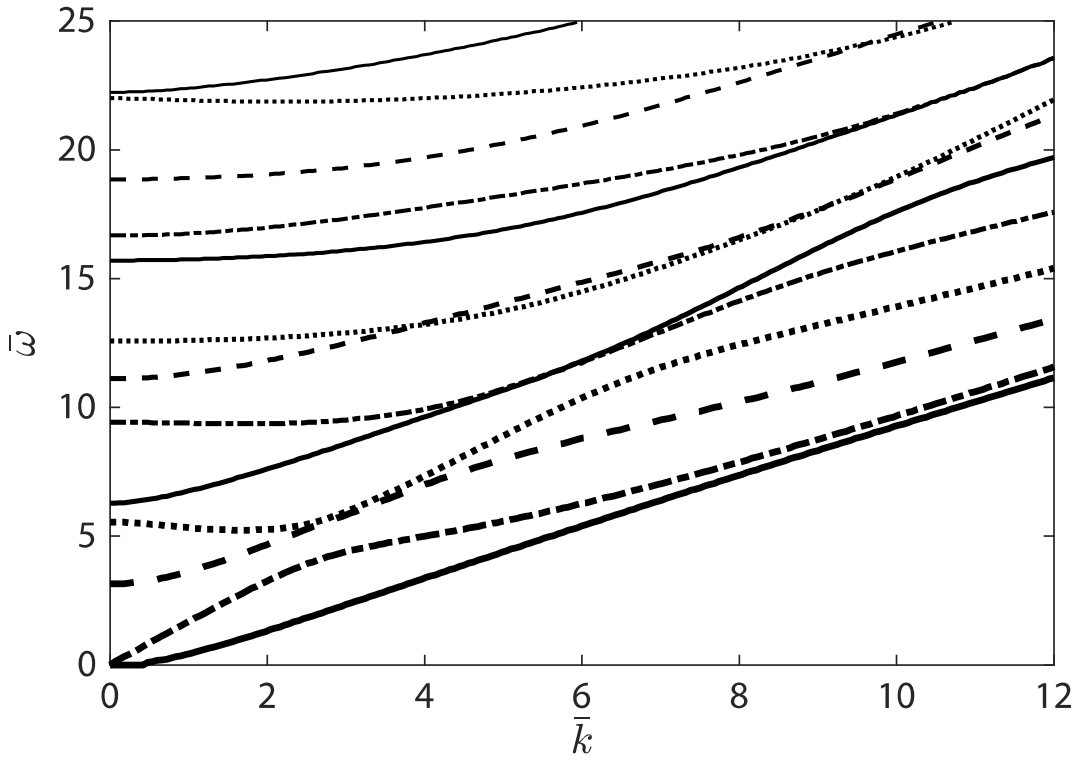


**Fig. 4.** Validation of the theoretical model and the numerical calculation. Replicate of dispersion curves are from Liu and Qu (1998)[34].

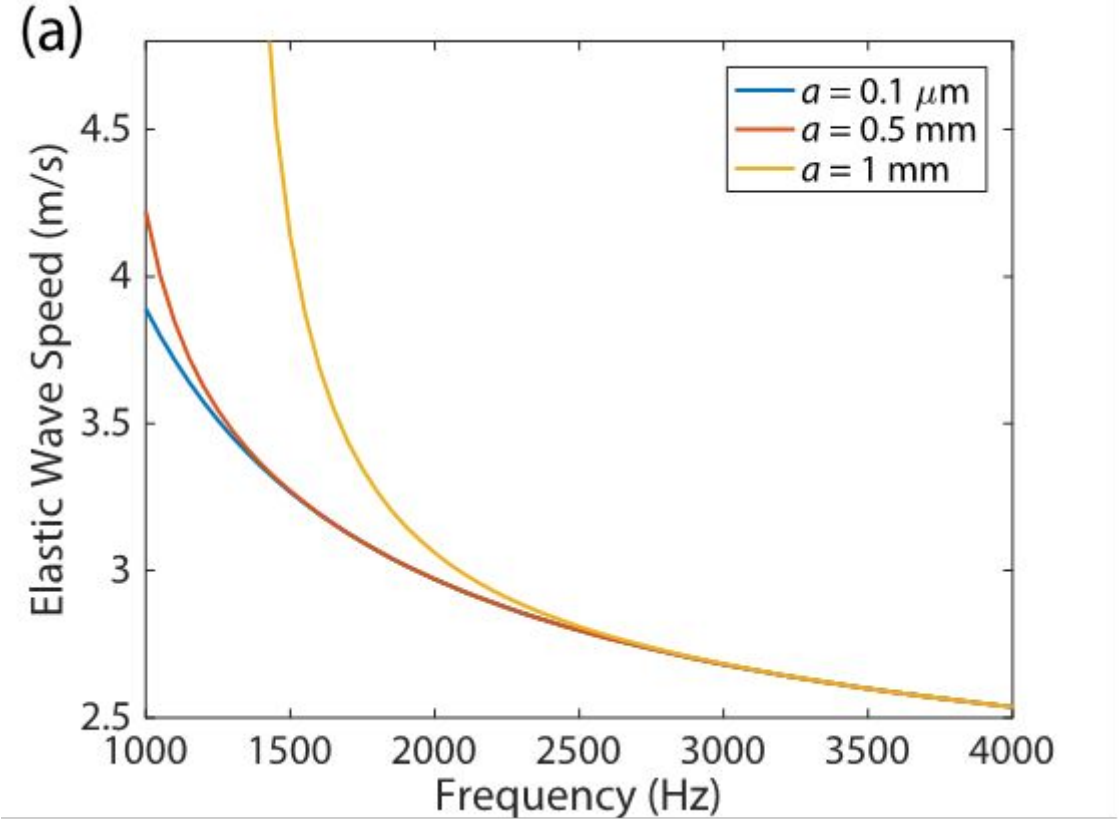
(a)
$a = 0.1\ \mu m$
$a = 0.5$ mm
$a = 1$ mm
Elastic Wave Speed (m/s)
4.5
4
3.5
3
2.5
1000
1500
2000
2500
3000
3500
4000
Frequency (Hz)

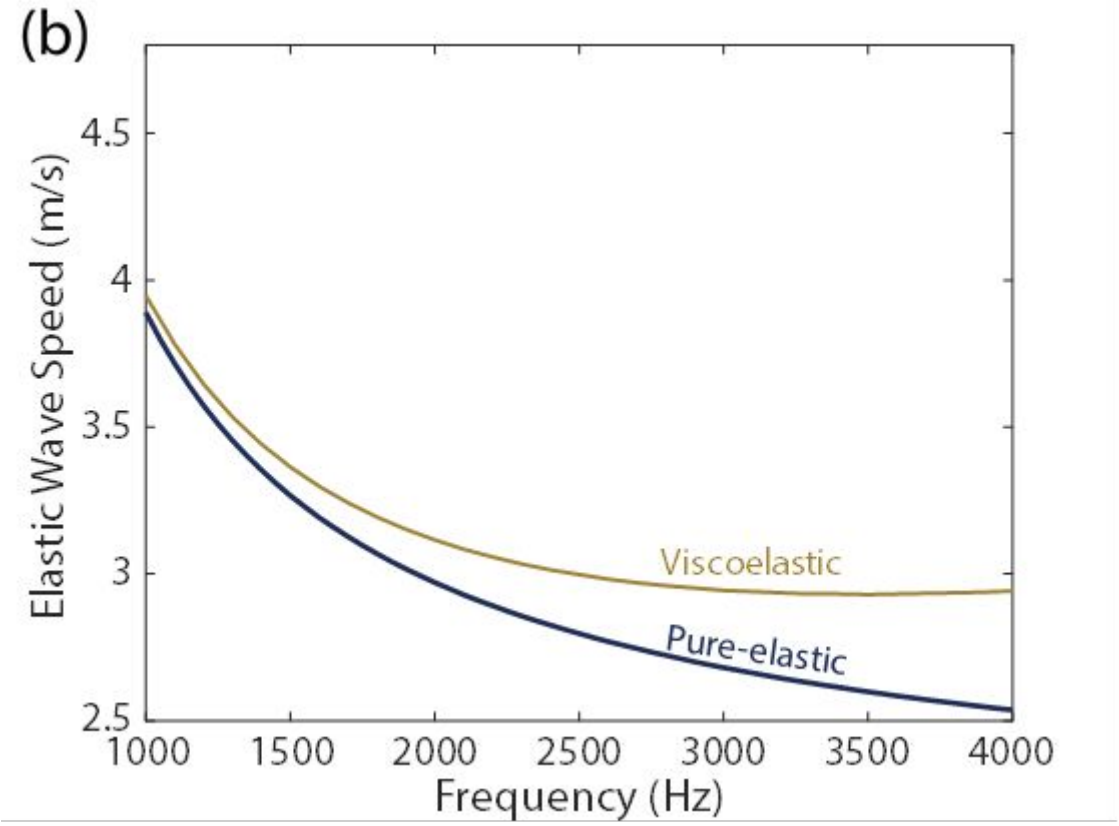
(b)
Elastic Wave Speed (m/s)
4.5
4
3.5
3
2.5
Viscoelastic
Pure-elastic
1000
1500
2000
2500
3000
3500
4000
Frequency (Hz)

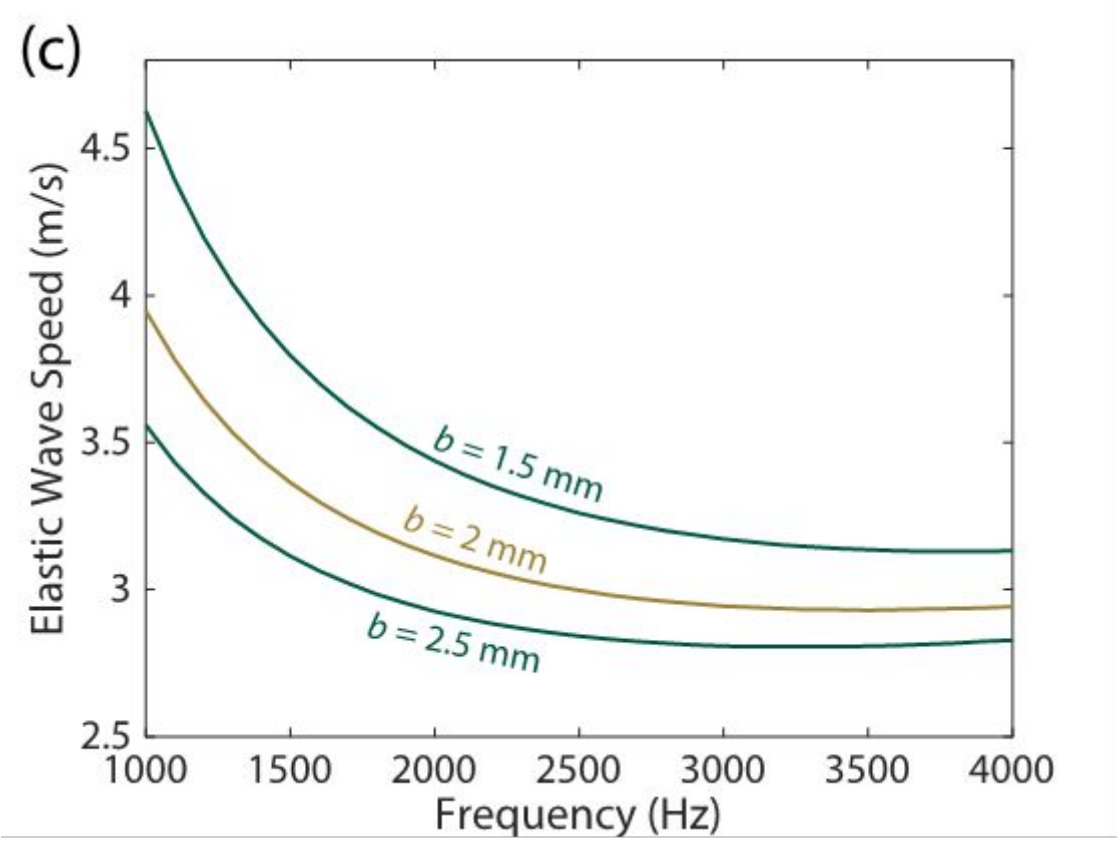


**Fig. 5.** Dispersion curve comparison for (a) different inner radii *a* with pure elastic properties (b) pure-elastic and viscoelastic properties, (b) different outer radii *b* with viscoelastic properties.

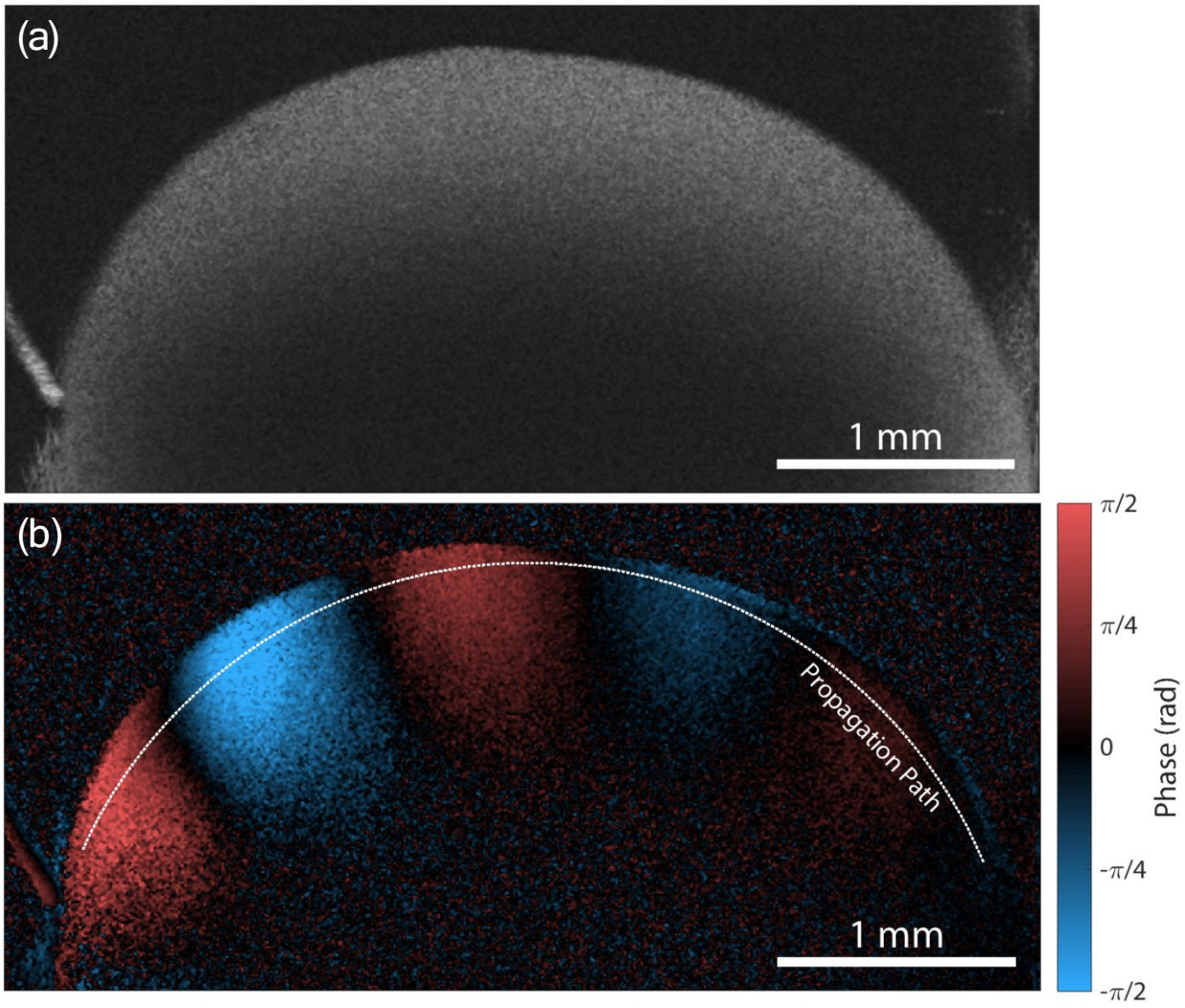


**Fig. 6.** (a) OCT image and (b) OCE image showing circumferential interface wave propagation in an alginate gel sphere. An animated GIF file can be found in the Electronic supplementary information.

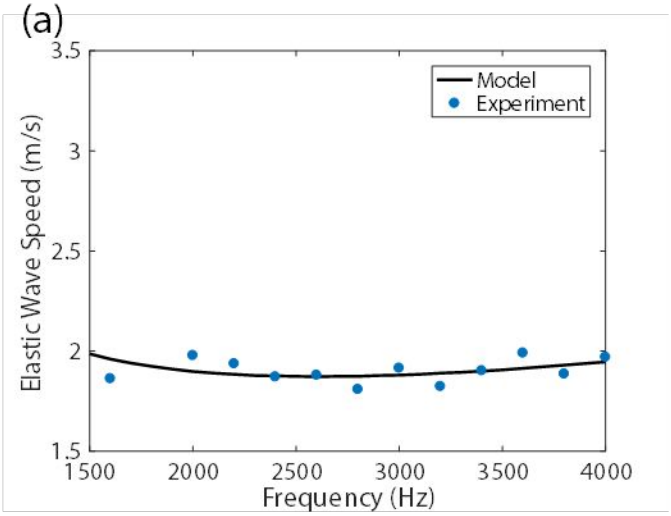
(a)
Model
Experiment
Elastic Wave Speed (m/s)
Frequency (Hz)
3.5
3
2.5
2
1.5
1500
2000
2500
3000
3500
4000

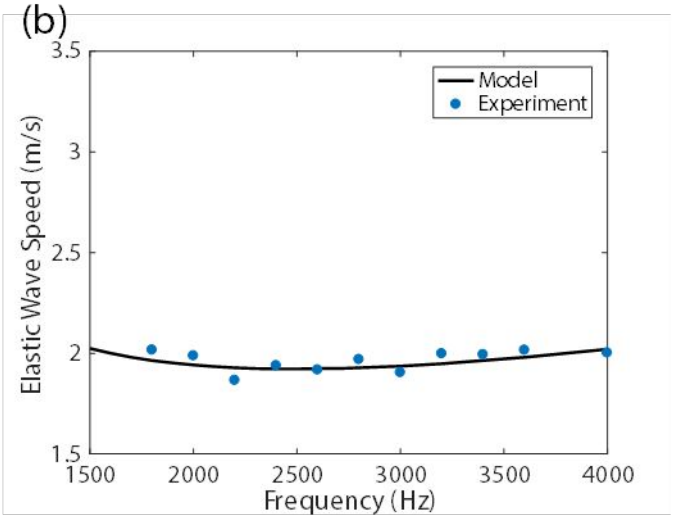
(b)
Model
Experiment
Elastic Wave Speed (m/s)
Frequency (Hz)
3.5
3
2.5
2
1.5
1500
2000
2500
3000
3500
4000

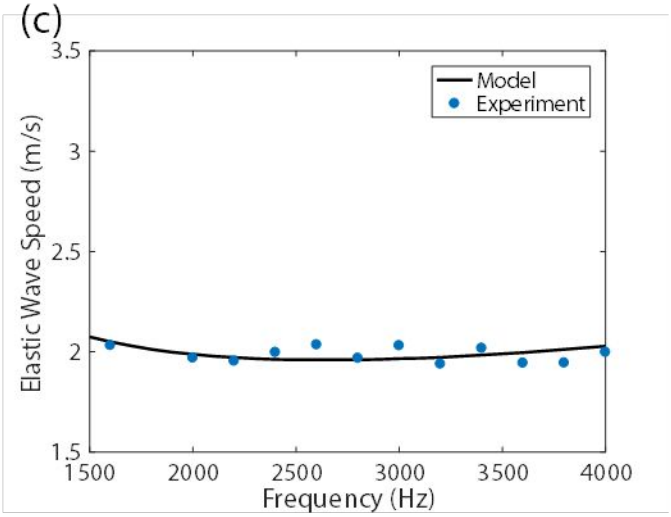
(c)
Model
Experiment
Elastic Wave Speed (m/s)
Frequency (Hz)
3.5
3
2.5
2
1.5
1500
2000
2500
3000
3500
4000

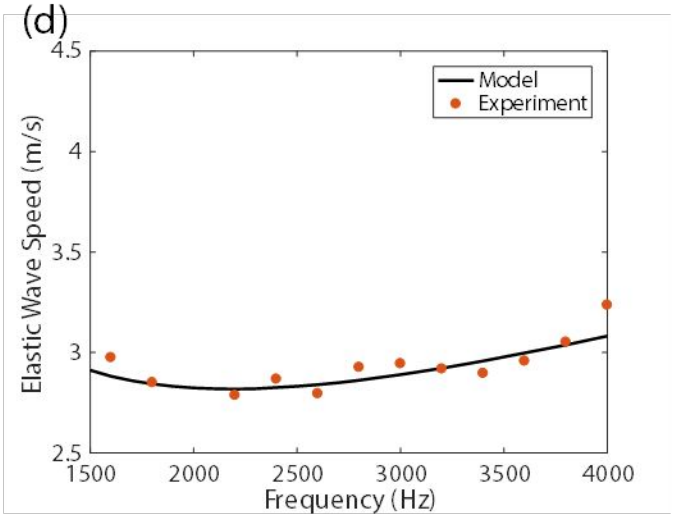
(d)
Model
Experiment
Elastic Wave Speed (m/s)
Frequency (Hz)
4.5
4
3.5
3
2.5
1500
2000
2500
3000
3500
4000

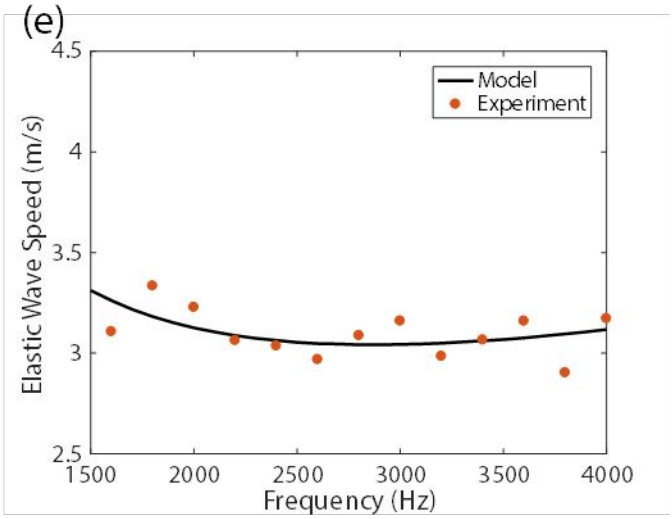
(e)
Model
Experiment
Elastic Wave Speed (m/s)
Frequency (Hz)
4.5
4
3.5
3
2.5
1500
2000
2500
3000
3500
4000

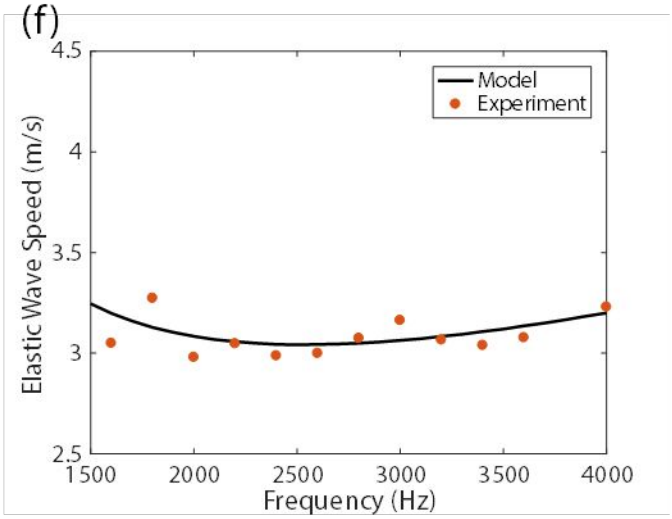
(f)
Model
Experiment
Elastic Wave Speed (m/s)
Frequency (Hz)
4.5
4
3.5
3
2.5
1500
2000
2500
3000
3500
4000

**Fig. 7.** Experimentally measured elastic wave speeds in alginate gel samples and the best-fit dispersion curves calculated by the theoretical model. Each figure corresponds to an individual sample with the alginate concentration of 0.8% (a, b, and c) and 1.2% (d, e, and f).

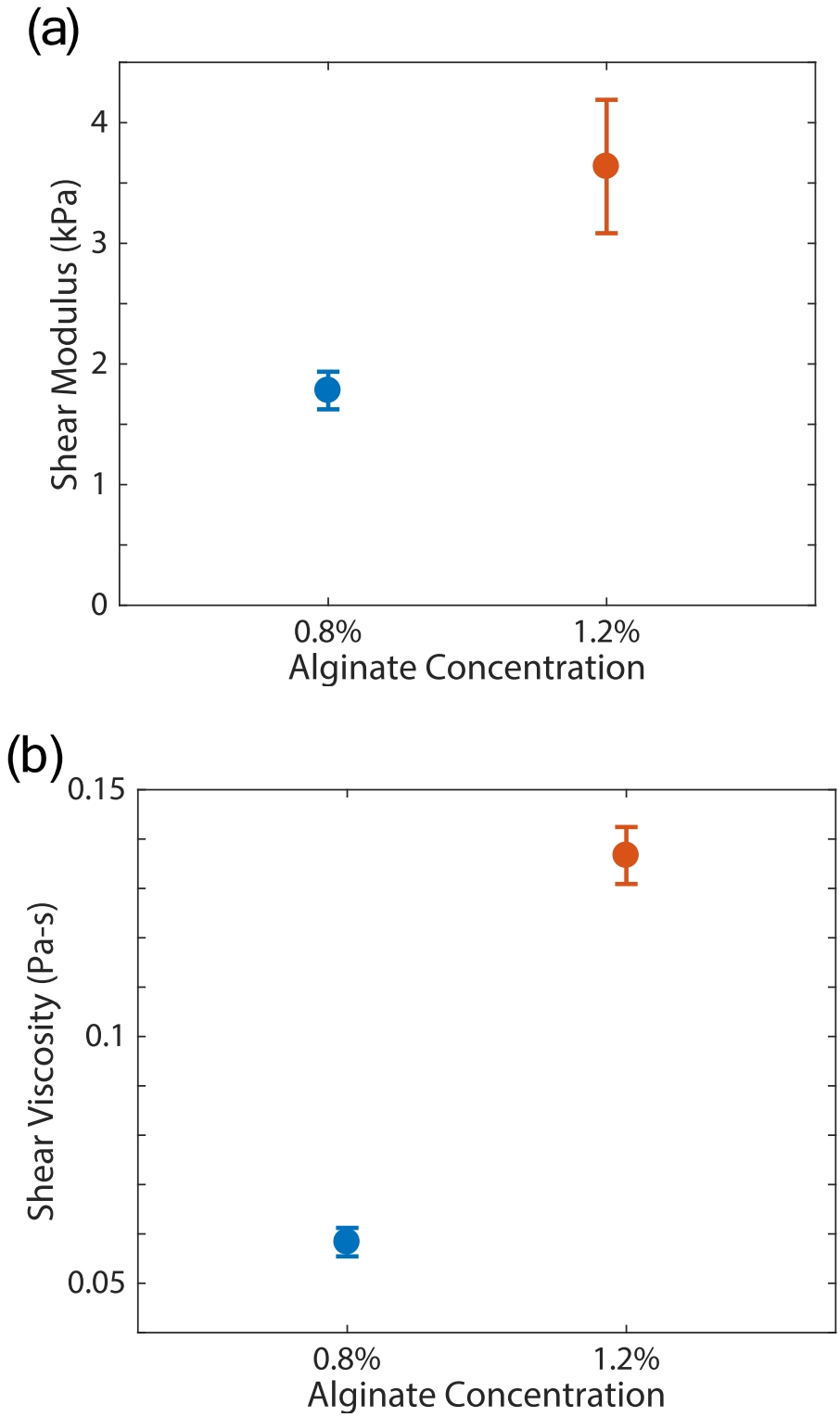


**Fig. 8.** Mean values (circles) and standard deviations (error bars) for (a) shear moduli and (b) shear viscosities estimated for alginate gel samples.

| **Sample properties** | (a) | (b) | (c) | (d) | (e) | (f) |
|---|---|---|---|---|---|---|
| Alginate concentration | 0.8% | 0.8% | 0.8% | 1.2% | 1.2% | 1.2% |
| Inner radius *a* (μm) | 0.1 | 0.1 | 0.1 | 0.1 | 0.1 | 0.1 |
| Outer radius *b* (mm) | 1.84 | 1.77 | 2.17 | 2.18 | 2.39 | 2.02 |
| Shear modulus (kPa) | 1.69 | 1.69 | 1.96 | 3.10 | 4.20 | 3.61 |
| Complex shear viscosity (Pa-s) | 0.055 | 0.06 | 0.06 | 0.14 | 0.13 | 0.14 |

**Table 1:** Model inputs and estimated mechanical properties for alginate gel samples.

| **Sample properties** | | |
|---|---|---|
| Alginate concentration | 0.8% | 1.2% |
| Mean shear modulus (kPa) | 1.78 | 3.64 |
| COV of shear modulus | 8.76% | 15.2% |
| Mean complex shear viscosity (Pa-s) | 0.058 | 0.137 |
| COV of complex shear viscosity | 4.95% | 4.22% |

**Table 2:** Mean values and variations of shear moduli and shear viscosities for alginate gel samples